

Molecular-bond breaking induced by interatomic decay processes

Ying-Chih Chiang,^{1,*} Selma Engin,² Peng Bao,^{3,†} Frank Otto,⁴ Přemysl Koloreňč,⁵ Petra Votavová,⁵
Tsveta Miteva,² Jiali Gao,^{6,7,‡} and Nicolas Sisourat^{2,§}

¹*School of Chemistry, University of Southampton, Highfield, Southampton SO17 1BJ, United Kingdom*

²*CNRS, Laboratoire de Chimie Physique - Matière et Rayonnement, Sorbonne Université, F-75005 Paris, France*


³*Beijing National Laboratory for Molecular Sciences (BNLMS), State Key Laboratory for Structural Chemistry of Unstable and Stable Species, Institute of Chemistry, Chinese Academy of Sciences, Zhongguancun, Beijing 100190, China*

⁴*Department of Chemistry, University College London, 20 Gordon Street, London WC1H 0AJ, United Kingdom*

⁵*Charles University, Faculty of Mathematics and Physics, Institute of Theoretical Physics, V Holešovičkách 2, 180 00 Prague, Czech Republic*

⁶*Shenzhen Bay Laboratory, and Lab of Computational Chemistry and Drug Design, Peking University Shenzhen Graduate School, Shenzhen, 518055, China*

⁷*Department of Chemistry and Supercomputing Institute, University of Minnesota, Minneapolis, Minnesota 55455, USA*

 (Received 29 April 2019; revised manuscript received 11 October 2019; published 11 November 2019)

Selective bond breaking in a molecule with the use of photons opens the way to control chemical reactions. We demonstrate here that dissociation of a molecule can be efficiently achieved by first photoexciting a neighboring atom or molecule. On the example of the giant He-H₂ dimer, we show that simultaneous ionization and excitation of the helium atom induces H₂ dissociation with a high probability. The excited He⁺ ion transfers its excess energy via interatomic Coulombic decay (ICD) or electron transfer mediated decay (ETMD) to H₂ which is then singly or doubly ionized, respectively. In both cases, the molecular ion dissociates effectively within a few tens of femtoseconds. Molecular-bond breaking induced by ICD and ETMD are expected to be general phenomena, which provide alternatives to standard photochemistry.

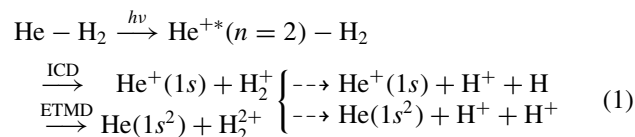
DOI: [10.1103/PhysRevA.100.052701](https://doi.org/10.1103/PhysRevA.100.052701)

I. INTRODUCTION

Absorption of light by molecules induces electronic and nuclear rearrangement. One of the ultimate goals of photochemistry is thus to selectively break a bond of a molecule with the use of photons [1,2]. This has been realized by acting directly on molecules through the use of combined light sources [3,4], shaped strong-field laser pulses (see [5–10] and references therein), or X-ray photons (see, for example, [11–13] and references therein).

In the present study, we demonstrate that breaking the covalent bond of a molecule can be efficiently achieved by first photoexciting a neighboring atom or molecule. Such an indirect process may be an alternative to standard photochemistry for embedded systems. On the example of the He-H₂ dimer, we show that simultaneous ionization and excitation of the helium atom induces H₂ dissociation with a high probability. Using accurate *ab initio* electronic structure calculations and quantum dynamical simulations, we reveal that the excited He⁺ ion transfers its excess energy via interatomic Coulombic decay (ICD) [14] to H₂, causing the ejection of an electron and yielding H₂⁺. While isolated H₂⁺ is stable, the presence of the nearby He⁺ leads to the dissociation of the molecular ion. Additionally, owing to electron transfer mediated decay (ETMD) and nonadiabatic couplings in the final states, charge

transfer between the species can take place leading to the creation of two protons and a neutral helium atom. The overall process can be described as follows:



ICD and ETMD are general and efficient nonradiative electronic deexcitation processes for atoms or molecules embedded in a chemical environment [14,15]. ICD was first measured in neon clusters following inner valence electron ionization [16,17]. Later, ICD was observed in water clusters [18–20]. Since these pioneer works, it was found in many diverse systems (see [20,21] for two recent reviews). One of its characteristics is that it rapidly (typically on the femtosecond time scale) creates two charges on neighboring species which leads to a strong Coulomb repulsion between these two species. ETMD has been also commonly found in weakly bound systems such as rare gas clusters [15,22–24] and in solutions [25] (see [26] for the complete bibliography on ICD and ETMD).

In this work, we have simulated fully quantum mechanically the ICD and ETMD processes in the giant He-H₂ dimer. Owing to the weak interaction between the helium and the hydrogen molecule and the low atomic masses, remarkable quantum effects take place: The nuclear wave function is exceptionally delocalized along the distance between the helium atom and the center of mass of the H₂ molecule, a so-called quantum halo state [27]. The distance between helium and

*Y.-C.Chiang@soton.ac.uk

†baopeng@iccas.ac.cn

‡jjiali@jialigao.org

§Nicolas.Sisourat@upmc.fr

H_2 can be up to about 50 Å. Furthermore, the probability density of this halo state has no noticeable dependence on the orientation of the H_2 molecule [28]. Owing to its relevance in astrophysics and its fundamental importance (as one of the simplest quantum systems), structure and energetics of the He- H_2 dimer have been thoroughly investigated [28–33].

II. THEORY

To investigate the possibility of a bond breaking process induced by ICD and ETMD, we consider only ionization and excitation of helium into the $2p$ orbitals since the state corresponding to $\text{He}^+(2s)$ should contribute less to the decay, as in [34]. Furthermore, we neglect the ICD channels leading to high excited states of H_2^+ since they correspond to higher order processes and their partial decay widths are thus expected to be small. We focus on a T-shape structure between the helium and the hydrogen molecule, i.e., with an angle of $\pi/2$ between the H_2 axis and the line joining the He and the center of mass of H_2 [35]. In the following, the H_2 bond length is denoted as r_{H_2} and the distance between the He atom and the H_2 center of mass is R .

In our calculations, we consider the following electronic states labeled according to their symmetry in the C_{2v} point group: The ground state He- H_2 ($^1\text{A}_1$), the ionized decaying states $\text{He}^{+*}(2p)\text{-H}_2$ ($^2\text{A}_1$, $^2\text{B}_1$ and $^2\text{B}_2$), the doubly-ionized singlet and triplet final states $\text{He}^+\text{-H}_2^+$ ($^1,^3\text{A}_1$), and the singlet final state He-H_2^{2+} ($^1\text{A}_1$). The potential energy surface of the ground-state He- H_2 dimer was taken from [31]. The surfaces of the decaying and triplet final electronic states have been computed using a fully correlated method (full configuration interaction method) with an aug-cc-pVDZ basis set [36,37], as implemented in the GAMESS-US *ab initio* program [38]. Similar to the lowest states of singly ionized He- H_2 [39], nonadiabatic couplings between the two singlet final electronic states take place. The corresponding potential energy surfaces and couplings have been determined using the multi-state density functional theory (MSDFT) [40–42]. In MSDFT, a set of spin-adapted valence bond-based diabatic states is constructed to form the active space. In the present study, altogether four states (two covalent and two ionic states) were used. They are (1) He^+ and the ground state of H_2^+ , (2) He^+ and the first excited state of H_2^+ , (3) the ground state of He and two protons, and (4) the first excited state of He and two protons. Then, the potential energy surfaces and couplings are obtained using the configuration interaction method. The MSDFT calculations were performed using a modified version of the GAMESS-US program. The PBE0 functional was used with the aug-cc-pVDZ basis set.

The decay widths were calculated with the Fano-ADC-Stieltjes method [43]. The partitioning of the configuration space into the bound states and continuum subspaces was performed using the generalized localization procedure as described in [44]. The calculations were carried out using the MOLCAS quantum chemistry package [45] and our own implementation of the ADC(2)_x method. The cc-pV6Z basis set [46] was used on all atoms. This basis set was augmented by [9s,9p,9d] and [8s,8p,8d] continuum-like Gaussian functions of Kaufmann-Baumeister-Jungen (KBJ) type [47] on the He atom and H atoms, respectively. Additional [5s,5p,5d]

KBJ basis set was placed at the center of mass of the cluster. This choice ensured both stable and convergent Stieltjes imaging procedures and good convergence of the resulting decay widths. The decay widths depend strongly on the distance between He and H_2 (see the Appendix) and only weakly on the H_2 bond length. We therefore include the R dependence of the widths in the nuclear dynamics calculations. The widths are, however, taken at the equilibrium distance of H_2 .

The nuclear dynamics of the ICD and ETMD processes were conducted using the time-dependent approach reported in [48,49]. In short, the ground-state nuclear wave packet is brought to the decaying electronic state according to the Franck-Condon principle. Owing to the weak interaction between He and H_2 in the neutral ground state, it is assumed that the dipole transition moment for the transition $\text{He} \rightarrow \text{He}^{+*}(2p) + e^-$ does not depend on the cluster geometry and is thus taken as a constant in our calculations. During its propagation on the decaying state, the wave packet gradually decays to the final electronic state. After the decay, the system is doubly charged and the corresponding potential energy surface is repulsive, the system thus dissociates. The nuclear dynamics has been performed with the Heidelberg multiconfigurational time-dependent Hartree (MCTDH) package [50–53] (see the Appendix for computational details). Complex absorbing potentials (CAPs) [54] are employed for the dissociative final states to account for the outgoing boundary conditions.

III. RESULTS AND DISCUSSION

The cuts of the potential energy surfaces at $r_{\text{H}_2} = 0.74$ Å and $R = 3.17$ Å are depicted in Fig. 1 (the two-dimensional potential energy surfaces are shown in the Appendix). Along R , the potential energy curve of the initial electronic ground state exhibits a minimum at $R = 3.17$ Å, which is about 1-meV deep. However, owing to the exceptional quantum nature of the system, the binding energy lies only a few μeV below the dissociation limit, resulting in an extremely delocalized nuclear wave function, as shown in the figure. After simultaneous excitation and ionization of helium, the nuclear wave function is promoted to one of the decaying states. The corresponding potential energy curves have a minimum around $R = 1.5\text{--}2$ Å. The nuclear wave packet therefore moves towards shorter R after the photoexcitation-ionization step. During this propagation, the wave packet decays gradually to the final electronic states. The potential energy curves of the latter are dissociative along R for the $\text{He}^+\text{-H}_2^+$ states owing to the Coulomb repulsion between these species, while the curve for He-H_2^{2+} exhibits a minimum around $R = 2$ Å. Along r_{H_2} the potential energy curves of the initial and decaying states are similar to that of isolated H_2 because the interaction with the helium atom is weak. The potential energy curve of the triplet and singlet $\text{He}^+\text{-H}_2^+$ final states have a minimum around $r_{\text{H}_2} = 1$ Å corresponding to the equilibrium distance of H_2^+ . However, for r_{H_2} larger than about 4 Å these potential energy curves become repulsive due to the presence of the nearby He^+ . The potential energy curve of the singlet He-H_2^{2+} is repulsive for all r_{H_2} distances.

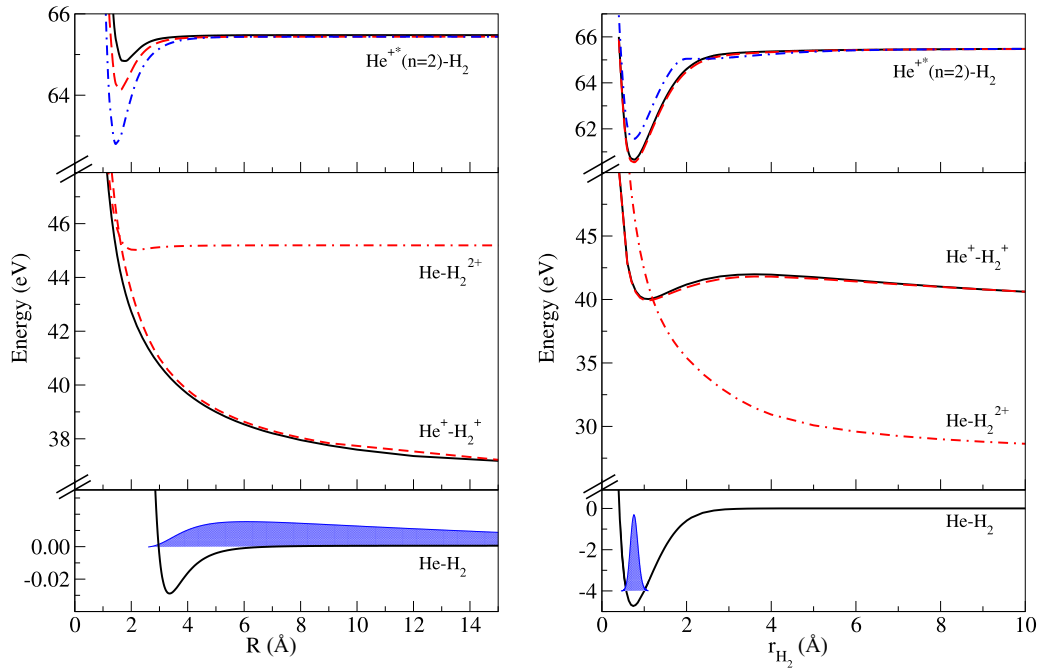


FIG. 1. Cuts of the potential energy surfaces and of the initial nuclear wave function at $r_{\text{H}_2} = 0.74 \text{ \AA}$ (left) and $R = 3.17 \text{ \AA}$ (right). In the left panel, the energies were shifted by the minimum of the isolated H_2 potential. The lower panels correspond to the electronic ground state of He-H_2 and the initial nuclear wave function. The upper panels show the cuts for the decaying states $\text{He}^{++}(2p)\text{-H}_2$ (A_1 in black line, B_1 in red dashed line, and B_2 in blue dashed-dotted line). The middle panels represent the triplet (black line), singlet $\text{He}^+\text{-H}_2^+$ (red dashed line), and He-H_2^{2+} (red dashed-dotted line) final electronic states. Two-dimensional potential energy surfaces are shown in the Appendix.

At this level of description it is already clear that ICD and ETMD can lead to two different three-body fragmentation channels: Either He^+ , H^+ , and H fragments or He , H^+ , and H^+ fragments are produced. In contrast, the usual Coulomb explosion after ICD leads to a two-body fragmentation, where the H_2^+ remains intact as a molecule. To go further, we have calculated the branching ratio of each channel using the nuclear dynamics simulations. In order to gain insights into the dissociation dynamics taking place after the electronic decay, we first show in Fig. 2 the time evolution of the nuclear probability density propagated on the triplet final state after decay from the A_1 decaying state. Before the decay, the wave packet had propagated on the A_1 state for 100 fs after the initial photoexcitation and ionization of the He atom. In this figure the time $\tau = 0$ fs corresponds to the moment of decay. Similar results are obtained for the other decaying states and for longer decay times. As seen in Fig. 2, after the decay H_2^+ is either left in highly excited vibrational levels or it dissociates. Indeed, the wave packet on the final state moves quickly to larger r_{H_2} distances: At $\tau = 10$ fs the wave packet is centered at $r_{\text{H}_2} = 2.5 \text{ \AA}$. By $\tau = 20$ fs a part of the wave packet has returned to shorter r_{H_2} distances (i.e., highly excited H_2^+) while another part continues to move towards asymptotic r_{H_2} distances (i.e., H_2 bond breaking). By $\tau = 30$ fs, the wave packet corresponding to vibrationally excited H_2^+ has moved away from the He^+ due to the mutual Coulomb repulsion while the other part of the wave function has reached large asymptotic r_{H_2} distances.

The decay probabilities for each decay channel are reported in Table I. Our quantum dynamics calculations show that, for each decaying state, about 90% of the nuclear wave

packet decays via ICD and ETMD. Within these pathways, we have evaluated the probability of each fragmentation channel. The branching ratios for the three decaying states and the three types of fragmentations (i.e., $\text{He}^+ + \text{H}_2^+$, $\text{He}^+ + \text{H}^+ + \text{H}$, and $\text{He} + \text{H}^+ + \text{H}^+$) are listed in Table I. For each channel, the contributions of the triplet and singlet final states are summed together. As seen in the table, the total branching ratio (i.e., average over all decaying states) of the three-body fragmentation channels is about 60%, illustrating the high efficiency of ICD

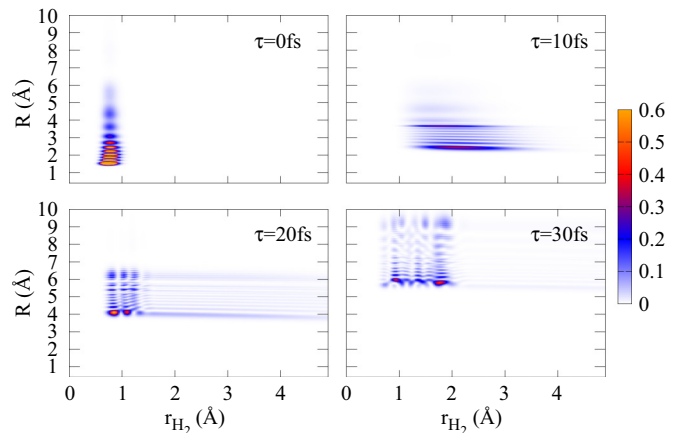


FIG. 2. Effective time evolution of the nuclear probability density propagated on the triplet final state $\text{He}^+\text{-H}_2^+$ after decay from the A_1 decaying state, whose wave packet had propagated for 100 fs after the initial ionization process. Here the time $\tau = 0$ fs corresponds to the moment of decay (see the Appendix for details).

TABLE I. Decay probabilities (in %) for each decay channel and branching ratios (in %) for the two-body and three-body fragmentations. For each symmetry, the branching ratios sum to 100% (i.e., the radiative decay is not included in the calculations of these branching ratios).

	A1	B1	B2
Radiative decay	11.9	11.7	10.0
ICD	62.4	51.3	46.6
ETMD	25.7	37.0	43.4
$\text{He}^+ + \text{H}_2^+$	45.1	35.9	48.9
$\text{He}^+ + \text{H} + \text{H}^+$	30.6	38.3	24.5
$\text{He} + \text{H}^+ + \text{H}^+$	24.3	25.8	26.6

and ETMD induced bond breaking. Among the three-body fragmentation channels, the two types, $\text{He}^+ + \text{H}^+ + \text{H}$ and $\text{He} + \text{H}^+ + \text{H}^+$, contribute nearly equally.

The results shown above are general and thus independent of any experimental scheme. However, to further illustrate the efficiency of ICD and ETMD induced bond breaking, it is relevant to discuss the competition with other processes in a typical photoionization experiment. In most experimental works on these relaxation processes, a single photon is used to initiate them. In the case of He-H_2 , a photon with energy above 65.4 eV is necessary to simultaneously ionize and excite the helium atom (see previous works on helium dimer [55,56]). For a photon energy around 70 eV, the ratio between the cross section for ionization excitation to $\text{He}^+(2p)$ and single ionization of helium is about 10% [57,58]. The single ionization cross section of helium in this energy range is around 1 Mbarn (see, for example, [59]). For comparison, at these photon energies the single ionization cross section of H_2 is about 10 times smaller and the ratio of dissociative ionization and nondissociative ionization of H_2 is around 25% [60–62]. ICD and ETMD induced H_2 bond breaking is therefore larger than what can be achieved with a single photon directly acting on H_2 . It should also be mentioned that direct double ionization of the He-H_2 dimer leading to

the same final states as the ones following ICD and ETMD is expected to be negligible: In the case of the helium dimer, which is similar to the present system, the efficiency of these decay processes is a few orders of magnitude larger than direct double ionization (see Fig. 2 in [63]). Furthermore, direct double ionization would not lead to the same fragments as the ones produced via ICD and ETMD because there is significant nuclear dynamics in the $\text{He}^+(2p)\text{-H}_2$ states which is essential to reach the final states in the region where H_2 bond breaking takes place.

IV. CONCLUSIONS

We have demonstrated that hydrogen molecular-bond breaking can be efficiently achieved by first ionizing and exciting the helium atom in the giant He-H_2 dimer. This indirect photodissociation process, which is mediated by ICD and ETMD, exhibits a branching ratio of more than 60%. He-H_2 has been employed in this work as a proof-of-principle system because it allows a very accurate theoretical description. However, molecular photodissociation induced by ICD and ETMD is expected to be general since the forces in play and the interatomic and molecular distances where the process takes place are similarly encountered in many systems in nature (see, for example, [64,65]). Our work shows that a better control of molecular photodissociation may be achieved through interatomic decay processes, opening thus new possibilities in photochemistry and photophysics.

ACKNOWLEDGMENTS

This project has received funding from Agence Nationale de la Recherche through Program No. ANR-16-CE29-0016-01. Y.-C.C. thanks the Royal Society for financial support (Grant No. NF171278). N.S. thanks Y. Gu and G. Quinchard for fruitful discussion. J.G. acknowledges financial support from the National Science Foundation of China (Grant No. 21533003). P.K. and P.V. acknowledge financial support from the Czech Science Foundation (Project GAGR No. 17-10866S).

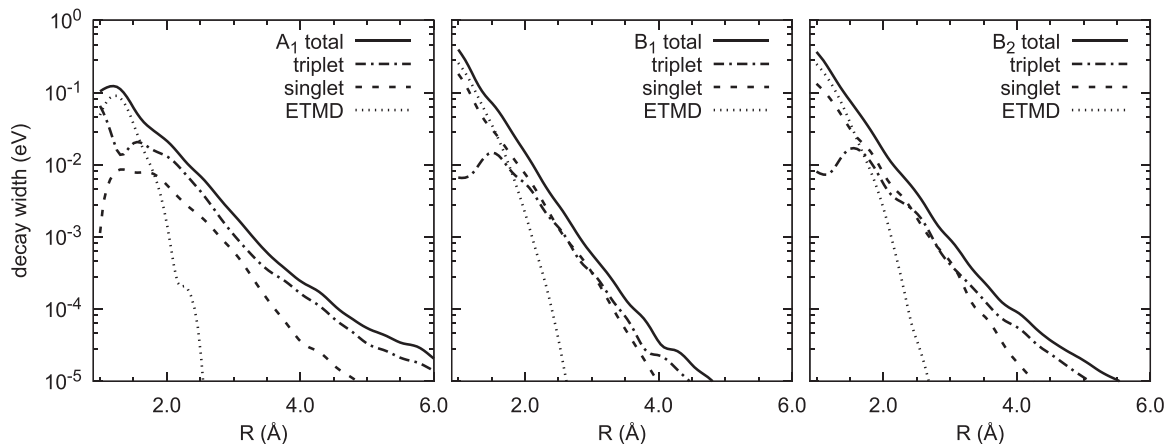


FIG. 3. R dependence of the decay widths from the decaying states A_1 (left), B_1 (middle), and B_2 (right) to the final states. The solid line shows the total decay width, while the dashed-dotted, dashed, and dotted lines show the partial decay widths to the triplet, singlet, and electron transfer mediated decay (ETMD) channels, respectively.

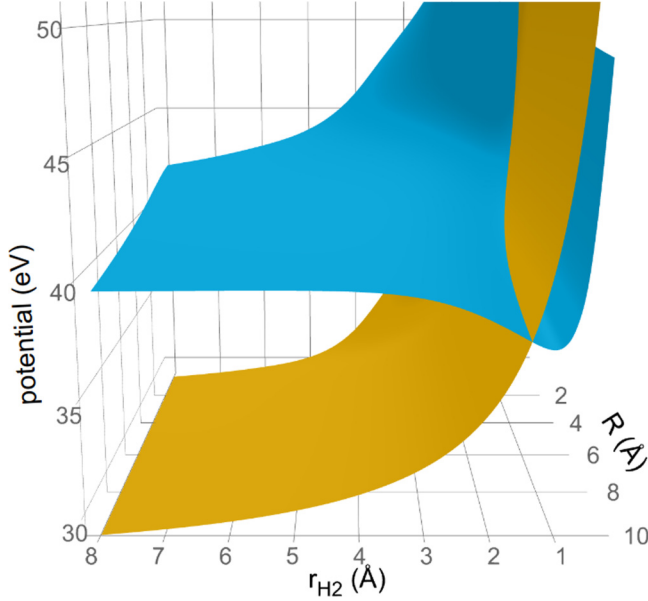


FIG. 4. Diabatic potential energy surfaces of the singlet final states [He^+-H_2^+ (blue) and $\text{He}-\text{H}_2^+$ (orange)].

APPENDIX: COMPUTATIONAL DETAILS

In the following, the doubly ionized singlet and triplet states of He^+-H_2^+ and the singlet state of $\text{He}-\text{H}_2^+$ are termed s , t , and α , respectively. As described in the main text, the two singlet final states s and α couple nonadiabatically. Since there is no coupling between the different decaying states, we have performed the calculations independently for each of them, and in the following d stands generically for one of the decaying states A_1 , B_1 , or B_2 .

Following the theoretical approach in [66], the nuclear wave packet's equations of motion on the populated electronic states throughout the process are given by

$$i|\dot{\psi}_d(t)\rangle = \left(\hat{H}_d - i \frac{\Gamma_d + \Gamma_{\text{ph}}}{2} \right) |\psi_d(t)\rangle, \quad (\text{A1a})$$

$$i|\dot{\psi}_t(E_e, t)\rangle = \hat{W}_{td} |\psi_d(t)\rangle + (\hat{H}_t + E_e) |\psi_t(E_e, t)\rangle, \quad (\text{A1b})$$

$$i|\dot{\psi}_s(E_e, t)\rangle = \hat{W}_{sd} |\psi_d(t)\rangle + (\hat{H}_s + E_e) |\psi_s(E_e, t)\rangle + \hat{V}_{s\alpha} |\psi_\alpha(E_e, t)\rangle, \quad (\text{A1c})$$

$$i|\dot{\psi}_\alpha(E_e, t)\rangle = \hat{W}_{\alpha d} |\psi_d(t)\rangle + (\hat{H}_\alpha + E_e) |\psi_\alpha(E_e, t)\rangle + \hat{V}_{\alpha s} |\psi_s(E_e, t)\rangle, \quad (\text{A1d})$$

where $|\psi_d(t)\rangle$ and $|\psi_{\{t,s,\alpha\}}(E_e, t)\rangle$ denote the nuclear wave packets of the decaying and final states, respectively, while E_e represents the energy of the emitted electron. The operators \hat{H}_x and \hat{W}_{fd} represent the Hamiltonian of state x and the transition matrix element from the decaying state d to the final state f .

The total decay width is denoted as Γ_d and that of the radiative decay as Γ_{ph} (the latter is taken from [55]). Finally, $\hat{V}_{s\alpha} = \hat{V}_{\alpha s}$ describes the coupling between the two singlet final states. The decay widths and the potential energy surfaces are shown in Fig. 3 and in Figs. 4 and 5, respectively.

As there is no coupling between the triplet and the singlet state, the propagation on the triplet final state (t) can be carried out independently. For the coupled singlet states (s and α) one can combine their final state wave functions into a two-component vector, and their respective Hamiltonians and transition matrix elements into a 2-by-2 matrix, so that Eqs. (A1c) and (A1d) can be combined into the form,

$$i|\dot{\psi}_f(E_e, t)\rangle = \hat{W}_{fd} |\psi_d(t)\rangle + (\hat{H}_f + E_e) |\psi_f(E_e, t)\rangle, \quad (\text{A2})$$

which is formally the same as Eq. (A1b) for the triplet state. In the following we use Eq. (A2) to discuss how to analyze the final state wave function ψ_f , which stands for either ψ_t or the two-component vector (ψ_s, ψ_α) .

We are interested in the branching ratios (BRs) for the possible dissociation channels, i.e., the two-body channel $\text{He}^+ + \text{H}_2^+$ or the three-body channels $\text{He}^+ + \text{H}^+ + \text{H}$ and $\text{He} + \text{H}^+ + \text{H}^+$. The BRs are directly proportional to how much of the final state wave packet reaches the respective asymptotic regions. To quantify this, we add to the final state Hamiltonian complex absorbing potentials (CAPs) which are placed outside the interaction region. The CAP terms have the form $-i\hat{W}_\gamma$ where γ stands for the dissociation channel, and \hat{W}_γ is real valued and non-negative. The loss (per time) of wave-function norm due to the CAP is given by $2\langle \psi_f(E_e, t) | \hat{W}_\gamma | \psi_f(E_e, t) \rangle$, so that the total amount of the wave function absorbed by the CAP in channel γ for the emitted electron energy E_e is given by

$$\text{BR}_\gamma(E_e) = 2 \int_0^\infty dt \langle \psi_f(E_e, t) | \hat{W}_\gamma | \psi_f(E_e, t) \rangle. \quad (\text{A3})$$

The CAPs are placed on both the R and r_{H_2} degrees of freedom. For the two-body channel the nuclear wave packet is absorbed by the CAP in the R direction, while for the three-body channels it is absorbed by the CAP in the r_{H_2} direction. Furthermore, for the singlet states we analyze the amount of wave function absorbed by the CAP on each state separately, in order to differentiate between the $\text{He}^+-\text{H}^+-\text{H}$ and the $\text{He}-\text{H}^+-\text{H}^+$ channels.

Here we are only interested in the total BRs, i.e., integrated over E_e , in which case the computation can be simplified so that no separate calculations for different values of E_e are required. Namely, Eq. (A2) has the formal solution,

$$|\psi_f(E_e, t)\rangle = -i \int_0^t dt' e^{-i(\hat{H}_f + E_e)(t-t')} \hat{W}_{fd} |\psi_d(t')\rangle. \quad (\text{A4})$$

Inserting into Eq. (A3) and integrating over E_e yields

$$\begin{aligned} \text{BR}_\gamma &= 2 \int dE_e \int_0^\infty dt \int_0^t dt' \int_0^{t'} dt'' \langle \psi_d(t') | \hat{W}_{fd} e^{i(\hat{H}_f + E_e)(t-t')} \hat{W}_\gamma e^{-i(\hat{H}_f + E_e)(t-t'')} \hat{W}_{fd} | \psi_d(t'') \rangle \\ &= 2 \int_0^\infty dt \int_0^t dt' \int_0^{t'} dt'' \int dE_e e^{-iE_e(t'-t'')} \langle \psi_d(t') | \hat{W}_{fd} e^{i\hat{H}_f(t-t')} \hat{W}_\gamma e^{-i\hat{H}_f(t-t'')} \hat{W}_{fd} | \psi_d(t'') \rangle \end{aligned}$$

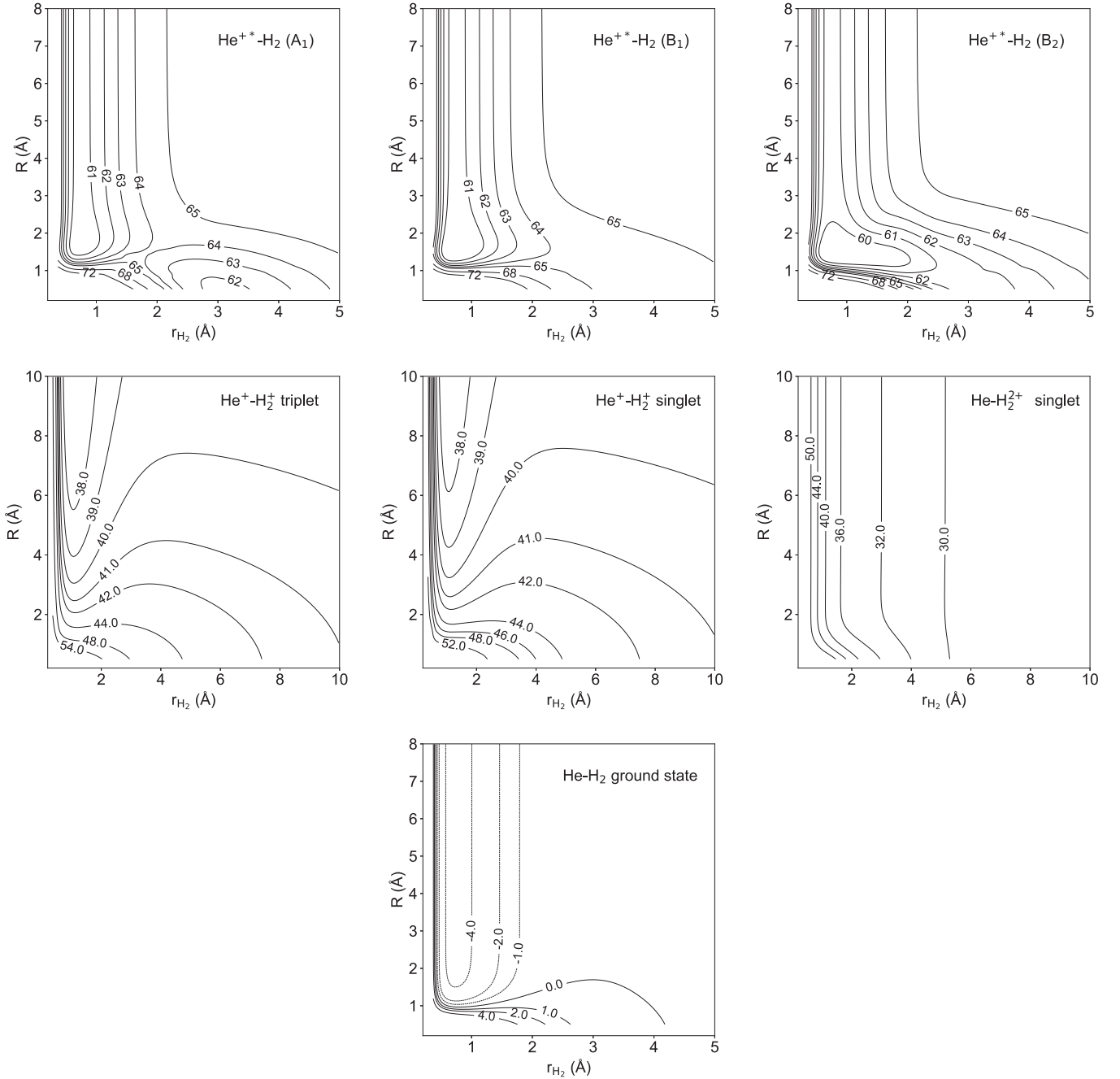


FIG. 5. Contour plots of the potential energy surfaces for the decaying states (top), final states (middle), and ground state (bottom). The contours are labeled by the potential energy in eV. The horizontal axis shows the H-H distance (r_{H_2}) while the vertical axis shows the He-H₂ distance (R), both in Ångstrom. Note that the final states are shown with a more extended coordinate range.

$$\begin{aligned}
 &= 4\pi \int_0^\infty dt \int_0^t dt' \langle \psi_d(t') | \hat{W}_{fd} e^{i\hat{H}_f(t-t')} \hat{W}_\gamma e^{-i\hat{H}_f(t-t')} \hat{W}_{fd} | \psi_d(t') \rangle \\
 &= 4\pi \int_0^\infty dt' \int_0^\infty d\tau \langle \psi_d(t') | \hat{W}_{fd} e^{i\hat{H}_f\tau} \hat{W}_\gamma e^{-i\hat{H}_f\tau} \hat{W}_{fd} | \psi_d(t') \rangle, \quad (A5)
 \end{aligned}$$

where in the last step we made use of the fact that $\int_0^\infty dt \int_0^t dt' = \int_0^\infty dt' \int_{t'}^\infty dt$ and we substituted $\tau = t - t'$. Defining the abbreviation $|\psi_f(\tau, t')\rangle =$

$\exp(-i\hat{H}_f\tau)\hat{W}_{fd}|\psi_d(t')\rangle$ we obtain

$$\text{BR}_\gamma = 4\pi \int_0^\infty dt' \int_0^\infty d\tau \langle \psi_f(\tau, t') | \hat{W}_\gamma | \psi_f(\tau, t') \rangle. \quad (A6)$$

In practice, the upper integral boundaries in Eq. (A6) are replaced by finite times such that (for the integral over τ) the matrix elements in Eq. (A6) become negligible, or such that (for the integral over t') the decaying state wave function $\psi_d(t')$ has negligible norm left.

Using this method, calculating the branching ratios only requires the computation of $|\psi_d(t)\rangle$ (“first propagation”) via Eq. (A1a) until t is large enough so that the state d is mostly depopulated, and subsequently computing $\exp(-i\hat{H}_f\tau)\hat{W}_{fd}|\psi_d(t')\rangle$ (“second propagation”) for a set of times t' such that the integral over t' in Eq. (A6) is converged. Notably, this approach avoids explicitly computing the time evolution of the final state wave packets as per Eqs. (A1b)–(A1d), which would be very computationally demanding as these would have to be solved for multiple values of the emitted electron energy, and would require a long time propagation as the decaying state wave packet $|\psi_d(t)\rangle$ [which enters as a source term into Eqs. (A1b)–(A1d)] only decays slowly. In contrast, the “second propagations” that are required for Eq. (A6) finish comparatively quickly as they can be stopped as soon as the wave packet $\exp(-i\hat{H}_f\tau)\hat{W}_{fd}|\psi_d(t')\rangle$ has been mostly absorbed by the CAP. On the other hand, this approach does not yield the actual time evolution on the final electronic states as described by Eqs. (A1b)–(A1d) for a particular electron energy, but an *effective* (integrated over E_e) time evolution on the final state that would happen if the wave packet from the decaying state would not decay gradually but instantaneously at the specific decay time t' . Figure 2 in the main text shows precisely this *effective* time evolution on the triplet final state for a decay from state A1 at $t' = 100$ fs.

Due to the nonadiabatic coupling between the two singlet final states, ICD and ETMD contribute to both three-body $\text{He}^+\text{-H}^+\text{-H}$ and $\text{He-H}^+\text{-H}^+$ fragmentation channels. In calculations of the BRs as presented in Table I, the contributions of the two transitions were added incoherently in each fragmentation channel. The reason for this choice is twofold. First, for correct coherent description, knowledge of the relative phase of the electronic wave functions after ICD and ETMD transitions is necessary. However, this information is not available in the *ab initio* Fano-ADC method. Only the partial decay widths $\Gamma_{fd} = 2\pi|W_{fd}|^2$ [66] are computed and the complex phases of the couplings W_{fd} are lost. Second, the phase depends on the molecular geometry. Since the decaying nuclear wave packets are broad, corresponding averaging over geometries is expected to lead to fast dephasing [67], supporting the incoherent description of the fragmentation process.

The quantum molecular dynamics computations for the above-mentioned “first” and “second” propagations are performed via the multiconfigurational time-dependent Hartree

TABLE II. Number of single-particle functions (SPFs) used for the MCTDH propagations on the given states, and duration of those propagations in fs. * More SPFs required for the $\text{B}_2 \rightarrow$ singlet decay.

State	Relaxation SPFs	First propagation		Second propagation	
		SPFS	duration/fs	SPFS ($t/s/\alpha$)	duration/fs
GS	8				
A ₁		8	100 000	15/15/15	300
B ₁		8	10 000	15/18/16	300
B ₂		8/10*	20 000	20/20/20	300

method [50–52] using the Heidelberg MCTDH software package [53].

Due to the dissociative nature of the ICD final state, large coordinate ranges with sufficiently small grid spacing must be employed in all degrees of freedom to account for the large kinetic energy that develops on the final states. Thus, the calculations were performed using 587 points of a sine discrete variable representation (DVR) to cover the range from 0.7 to 30.0 bohr for r_{H_2} , while 2048 grid points of a fast-Fourier transform (FFT) representation are employed for R to cover the range from 0.95 to 103.30 bohr. Only the decay from B_2 to the singlet final state requires 3072 FFT points to account for a larger nuclear kinetic energy encountered during the dissociation.

The initial wave packet was created via relaxing a Gaussian wave packet centered at $r_{\text{H}_2} = 1.449$ bohr and $R = 20.0$ bohr, using eight single-particle functions (SPFs), and convergence was determined by the ground-state energy being stable to within 10^{-9} eV. This ground-state wave packet was then directly placed (vertical excitation) onto the PES of the decaying state d (being either A_1 , B_1 , or B_2) where the “first” propagation according to Eq. (A1a) was carried out in order to obtain $|\psi_d(t)\rangle$. The Hamiltonian for state d was augmented with a CAP in the R degree of freedom in order to capture the small amount of the wave packet that undergoes direct dissociation in the intermediate state. Here we also employed eight SPFs for all decaying states, except for the aforementioned B_2 -to-singlet channel, where 10 SPFs are required. Propagation times on the d states are listed in Table II. We note that the propagation on the A_1 state takes significantly longer, as the decay from this state is slower due to the smaller decay width (cf. Fig. 3). The “second” propagation for computing $\exp(-i\hat{H}_f\tau)\hat{W}_{fd}|\psi_d(t')\rangle$ generally requires more SPFs; see Table II for details. These propagations had to be carried out for multiple values of the decay time t' such that the integral over t' in Eq. (A6) could be calculated. We found that carrying out this integral with a step size of $\Delta t' = 40$ fs was sufficient to obtain converged results.

- [1] A. H. Zewail, *Phys. Today* **33**(11), 27 (1980).
 [2] W. S. Warren, H. Rabitz, and M. Dahleh, *Science* **259**, 1581 (1993).
 [3] F. F. Crim, *Science* **249**, 1387 (1990).
 [4] F. F. Crim, *J. Phys. Chem.* **100**, 12725 (1996).
 [5] R. N. Zare, *Science* **279**, 1875 (1998).

- [6] A. Assion, T. Baumert, M. Bergt, T. Brixner, B. Kiefer, V. Seyfried, M. Strehle, and G. Gerber, *Science* **282**, 919 (1998).
 [7] R. J. Levis, G. M. Menkir, and H. Rabitz, *Science* **292**, 709 (2001).
 [8] N. V. Vitanov, T. Halfmann, B. W. Shore, and K. Bergmann, *Annu. Rev. Phys. Chem.* **52**, 763 (2001).

- [9] C. Brif, R. Chakrabarti, and H. Rabitz, *New J. Phys.* **12**, 075008 (2010).
- [10] I. R. Solá, J. González-Vázquez, R. de Nalda, and L. Bañares, *Phys. Chem. Chem. Phys.* **17**, 13183 (2015).
- [11] W. Eberhardt, T. K. Sham, R. Carr, S. Krummacher, M. Strongin, S. L. Weng, and D. Wesner, *Phys. Rev. Lett.* **50**, 1038 (1983).
- [12] R. Romberg, N. Heckmair, S. P. Frigo, A. Ogurtsov, D. Menzel, and P. Feulner, *Phys. Rev. Lett.* **84**, 374 (2000).
- [13] L. Inhester, B. Oostenrijk, M. Patanen, E. Kokkonen, S. H. Southworth, C. Bostedt, O. Travnikova, T. Marchenko, S.-K. Son, R. Santra, M. Simon, L. Young, and S. L. Sorensen, *J. Phys. Chem. Lett.* **9**, 1156 (2018).
- [14] L. S. Cederbaum, J. Zobeley, and F. Tarantelli, *Phys. Rev. Lett.* **79**, 4778 (1997).
- [15] J. Zobeley, R. Santra, and L. S. Cederbaum, *J. Chem. Phys.* **115**, 5076 (2001).
- [16] S. Marburger, O. Kugeler, U. Hergenhahn, and T. Möller, *Phys. Rev. Lett.* **90**, 203401 (2003).
- [17] T. Jahnke, A. Czasch, M. S. Schöffler, S. Schössler, A. Knapp, M. Käsz, J. Titze, C. Wimmer, K. Kreidi, R. E. Grisenti *et al.*, *Phys. Rev. Lett.* **93**, 163401 (2004).
- [18] M. Mucke, M. Braune, S. Barth, M. Förstel, T. Li., Volker Ulrich, T. Arion, U. Becker, A. Bradshaw, and U. Hergenhahn, *Nat. Phys.* **6**, 143 (2010).
- [19] T. Jahnke, H. Sann, T. Havermeier, K. Kreidi, C. Stuck, M. Meckel, M. Schöffler, N. Neumann, R. Wallauer, S. Voss *et al.*, *Nat. Phys.* **6**, 139 (2010).
- [20] U. Hergenhahn, *J. Electron Spectrosc. Relat. Phenom.* **184**, 78 (2011).
- [21] T. Jahnke, *J. Phys. B: At. Mol. Opt. Phys.* **48**, 082001 (2015).
- [22] K. Sakai, S. Stoychev, T. Ouchi, I. Higuchi, M. Schöffler, T. Mazza, H. Fukuzawa, K. Nagaya, M. Yao, Y. Tamenori, A. I. Kuleff, N. Saito, and K. Ueda, *Phys. Rev. Lett.* **106**, 033401 (2011).
- [23] M. Förstel, M. Mucke, T. Arion, A. M. Bradshaw, and U. Hergenhahn, *Phys. Rev. Lett.* **106**, 033402 (2011).
- [24] D. You, H. Fukuzawa, Y. Sakakibara, T. Takanashi, Y. Ito, G. G. Maliyar, K. Motomura, K. Nagaya, T. Nishiyama, K. Asa, Y. Sato, N. Saito, M. Oura, M. Schöffler, G. Kastirke, U. Hergenhahn, V. Stumpf, K. Gokhberg, A. I. Kuleff, L. S. Cederbaum, and K. Ueda, *Nat. Commun.* **8**, 14277 (2017).
- [25] I. Unger, R. Seidel, S. Thürmer, M. N. Pohl, E. F. Aziz, L. S. Cederbaum, E. Muchová, P. Slavíček, B. Winter, and N. V. Kryzhevoi, *Nat. Chem.* **9**, 708 (2017).
- [26] [<http://www.pci.uni-heidelberg.de/tc/usr/icd/ICD.refbase.html>].
- [27] A. S. Jensen, K. Riisager, E. Garrido, and D. V. Fedorov, *Rev. Mod. Phys.* **76**, 215 (2004).
- [28] F. A. Gianturco, T. González-Lezana, G. Delgado-Barrio, and P. Villarreal, *J. Chem. Phys.* **122**, 084308 (2005).
- [29] P. Muchnick and A. Russek, *J. Chem. Phys.* **100**, 4336 (1994).
- [30] F.-M. Tao, *J. Chem. Phys.* **100**, 4947 (1994).
- [31] A. I. Boothroyd, P. G. Martin, and M. R. Peterson, *J. Chem. Phys.* **119**, 3187 (2003).
- [32] P. Barletta, *Eur. Phys. J. D* **53**, 33 (2009).
- [33] D. Rapp, A. G. Csaszar, K. Yamamouchi, and T. Szidarouszky, *J. Chem. Theory Comput.* **14**, 1523 (2018).
- [34] S. Kazandjian, J. Rist, M. Weller, F. Wiegandt, D. Asliturk, S. Grundmann, M. Kircher, G. Nalin, D. Pitters, I. VelaPerez *et al.*, *Phys. Rev. A* **98**, 050701(R) (2018).
- [35] Owing to the extreme delocalization of the nuclear wave function, a full three-dimensional quantum dynamics simulation is out of reach. However, we have performed semiclassical dynamics in three dimensions. The latter agree well with the quantum dynamics simulation for the T-shape geometry. Furthermore, the conclusions presented here remain correct when including the third dimension. The semiclassical dynamics simulations will be reported in a later publication.
- [36] T. H. Dunning, *J. Chem. Phys.* **90**, 1007 (1989).
- [37] D. E. Woon and T. H. Dunning, *J. Chem. Phys.* **100**, 2975 (1994).
- [38] M. W. Schmidt, K. K. Baldrige, J. A. Boatz, S. T. Elbert, M. S. Gordon, J. H. Jensen, S. Koseki, N. Matsunaga, K. A. Nguyen, S. J. Su, T. L. Windus, M. Dupuis, and J. A. Montgomery, *J. Comput. Chem.* **14**, 1347 (1993).
- [39] D. De Fazio, A. Aguado, and C. Petrongolo, *Front. Chem.* **7**, 249 (2019).
- [40] A. Cembran, L. Song, Y. Mo, and J. Gao, *J. Chem. Theory Comput.* **5**, 2702 (2009).
- [41] J. Gao, A. Grofe, H. Ren, and P. Bao, *J. Phys. Chem. Lett.* **7**, 5143 (2016).
- [42] A. Grofe, X. Chen, W. J. Liu, and J. Gao, *J. Phys. Chem. Lett.* **8**, 4838 (2017).
- [43] V. Averbukh and L. S. Cederbaum, *J. Chem. Phys.* **123**, 204107 (2005).
- [44] P. Kolorenč and N. Sisourat, *J. Chem. Phys.* **143**, 224310 (2015).
- [45] F. Aquilante, L. De Vico, N. Ferré, G. Ghigo, P.Å. Malmqvist, P. Neogrády, T. Bondo Pedersen, M. Pitoňák, M. Reiher, B. O. Roos, L. Serrano-Andrés *et al.*, *J. Comput. Chem.* **31**, 224 (2010).
- [46] T. Van Mourik, A. K. Wilson, and T. H. Dunning, *Mol. Phys.* **96**, 529 (1999).
- [47] K. Kaufmann, W. Baumeister and M. Jungen, *J. Phys. B: At., Mol. Opt. Phys.* **22**, 2223 (1989).
- [48] L. S. Cederbaum and F. Tarantelli, *J. Chem. Phys.* **98**, 9691 (1993).
- [49] Y.-C. Chiang, F. Otto, H.-D. Meyer, and L. S. Cederbaum, *Phys. Rev. Lett.* **107**, 173001 (2011).
- [50] H.-D. Meyer, U. Manthe, and L. S. Cederbaum, *Chem. Phys. Lett.* **165**, 73 (1990).
- [51] H.-D. Meyer, F. Gatti, and G. A. Worth, *Multidimensional Quantum Dynamics: MCTDH Theory and Applications* (Wiley, Weinheim, 2009).
- [52] M. H. Beck, A. Jäckle, G. A. Worth and H.-D. Meyer, *Phys. Rep.* **324**, 1 (2000).
- [53] G. A. Worth, M. H. Beck, A. Jäckle, and H.-D. Meyer, Computer code MCTDH, Version 8.4 (2007); see [<http://mctdh.uni-hd.de>].
- [54] R. Kosloff and D. Kosloff, *J. Comput. Phys.* **63**, 363 (1986).
- [55] N. Sisourat *et al.*, *Nat. Phys.* **6**, 508 (2010).
- [56] T. Havermeier, T. Jahnke, K. Kreidi, R. Wallauer, S. Voss, M. Schöffler, S. Schössler, L. Foucar, N. Neumann, J. Titze *et al.*, *Phys. Rev. Lett.* **104**, 133401 (2010).
- [57] P. R. Woodruff and J. A. R. Samson, *Phys. Rev. A* **25**, 848 (1982).

- [58] R. Wehlitz, I. A. Sellindag, O. Hemmersddag, S. B. Whitfieldddag, P. Glansddag, H. Wangddag, D. W. Lindleddag, B. Langer, N. Berrah, J. Viefhaus and U. Becker, *J. Phys. B: At., Mol. Opt. Phys.* **30**, L51 (1997).
- [59] G. V. Marr and J. B. West, *At. Dat. Nuc. Dat. Tab.* **18**, 497 (1976).
- [60] Y. M. Chung, E. M. Lee, T. Masuoka, and James A. R. Samson, *J. Chem. Phys.* **99**, 885 (1993).
- [61] M. Yan, H. R. Sadeghpour, and A. Dalgarno, *ApJ* **496**, 1044 (1998).
- [62] A. Palacios, H. Bachau, and F. Martín, *Phys. Rev. Lett.* **96**, 143001 (2006).
- [63] P. Burzynski, F. Trinter, J. B. Williams, M. Weller, M. Waitz, M. Pitzer, J. Voigtsberger, C. Schober, G. Kastirke, C. Muller *et al.*, *Phys. Rev. A* **90**, 022515 (2014).
- [64] V. Stumpf, K. Gokhberg, and L. S. Cederbaum, *Nat. Chem.* **8**, 237 (2016).
- [65] A. Ghosh, L. S. Cederbaum, and K. Gokhberg, *J. Chem. Phys.* **150**, 164309 (2019).
- [66] E. Pahl, H.-D. Meyer, and L. S. Cederbaum, *Z. Phys. D* **38**, 215 (1996).
- [67] M. Vacher, L. Steinberg, A. J. Jenkins, M. J. Bearpark, and M. A. Robb, *Phys. Rev. A* **92**, 040502(R) (2015).